

A Search for Subkilometer-sized Ordinary Chondrite Like Asteroids in the Main-Belt

H. W. Lin^a, Fumi Yoshida^b, Y. T. Chen^c, W. H. Ip^{a,d}, C. K. Chang^a

^a*Institute of Astronomy, National Central University, Taoyuan 32001, Taiwan*

^b*National Astronomical Observatory of Japan, 2-21-1 Osawa, Mitaka, Tokyo 181-8588, JAPAN*

^c*Institute of Astronomy and Astrophysics, Academia Sinica, P. O. Box 23-141, Taipei 106, Taiwan*

^d*Space Science Institute, Macau University of Science and Technology, Taipa, Macau*

Abstract

The size-dependent effects of asteroids on surface regolith and collisional lifetimes suggest that small asteroids are younger than large asteroids. In this study, we performed multicolor main-belt asteroid (MBA) survey by Subaru telescope/Suprime-Cam to search for subkilometer-sized ordinary chondrite (Q-type) like MBAs. The total survey area was 1.5 deg^2 near ecliptic plane and close to the opposition. We detected 150 MBAs with 4 bands (B , V , R , I) in this survey. The range of absolute magnitude of detected asteroids was between 13 and 22 magnitude, which is equivalent to the size range of kilometer to sub-kilometer diameter in MBAs.

From this observation, 75 of 150 MBAs with color uncertainty less than 0.1 were used in the spectral type analysis, and two possible Q-type asteroids were detected. This mean that the Q-type to S-type ratio in MBAs is < 0.05 . Meanwhile, the Q/S ratio in near Earth asteroids (NEAs) has been estimated to be 0.5 to 2 (Binzel et al., 2004; Dandy et al., 2003). Therefore, Q-type NEAs might be delivered from the main belt region with weathered, S-type surface into near Earth region and then obtain their Q-type, non-weathered surface after undergoing re-surfacing process there. The resurfacing mechanisms could be: 1. dispersal of surface material by tidal effect during planetary encounters (Binzel et al., 2010; Nesvorný et al., 2010), 2. the YORP spin-up induced rotational-fission (Polishook et al., 2014) or surface re-arrangement, or 3. thermal degradation (Delbo et al., 2014).

Keywords:

1. Introduction

The taxonomic type of asteroid has been studied extensively to understand the mineral composition of asteroids. It is mostly based on the asteroid's colors and spectra in optical wavelength. Numerous types (such as S, C, D, B and V) have been identified (Bowell et al., 1978; Tholen, 1984; Zellner et al., 1985; Bus and Binzel, 2002a,b; DeMeo et al., 2009; DeMeo and Carry, 2013, 2014). Space weathering effects and related color-spectrum correlations for the main-belt asteroids (MBAs) and near-Earth asteroids (NEAs) have also been studied (Chapman, 1996; Binzel et al., 2001; Chapman, 2004; Clark et al., 2001; Jedicke et al., 2004; Nesvorný et al., 2005; Willman et al., 2008, 2010; Willman and Jedicke, 2011; Thomas et al., 2012). These studies have been primarily based on relatively larger asteroids; only few studies done for kilometer to sub-kilometer asteroids because of the requirement of large telescopes to determine their colors or spectra, have been conducted.

Asteroids with sizes below the kilometer range are most likely collisional fragments of large asteroids (Davis et al., 2002; Morbidelli et al., 2009). Therefore, their surfaces should have lower degree of space weathering compared with larger asteroids, which have survived throughout the history of the solar system (Binzel et al., 2001, 2004; Bus and Binzel, 2002b). Some small, several hundred meter sized NEAs observed in detail while during close approach to the Earth, showed Q-type spectra which are similar to those of the ordinary chondrite (OC) with low degree of space weathering (Tholen, 1984). Researchers also reported that a spectral transition could occur between S-type and Q-type asteroids (Binzel et al., 1996, 2004; Dandy et al., 2003). These results indicated that S-type asteroids are likely Q-type asteroids, with their surface materials originally characterized by OC-like spectra, but modified by space weathering to the present-day darker and redder spectra. Laboratory experiments (Sasaki et al., 2001; Brunetto et al., 2006) and observations conducted by the NEAR and Hayabusa space missions (Clark et al., 2002; Ishiguro et al., 2007) supported this theory.

A large number of Q-type asteroids have been detected in the near-Earth region (Binzel et al., 2001; Dandy et al., 2003; Stuart and Binzel, 2004; DeMeo and Carry, 2013), the ratio of Q/S in NEAs is 0.5 to 2. If Q-type NEAs were produced by collisions, we should also detect Q-type MBAs because the collisional rate

in main-belt is higher than that in near-Earth region. While, Q-type asteroids were missing in the main-belt in the earlier studies (Bus and Binzel, 2002a,b; Lazzaro et al., 2004), more recent observations have detected several Q-type MBAs in the extremely young asteroid family “Datura dynamical cluster” (Mothé-Diniz and Nesvorný, 2008) and the older Koronis family (Rivkin et al., 2011; Thomas et al., 2011). Carvano et al. (2010) classed 3296 of 62576 asteroids as Q-type-like objects in SDSS Moving Object Catalog (SDSSMOC4). Polishook et al. (2014) also detect two Q-type asteroids, (19289) 1996 HY12 and (54827) 2001 NQ8, in the unbound asteroid pairs. These results show that Q-type taxonomy is not limited to the NEA population. However, the abundance of Q-type asteroids in the main-belt is still low comparing with that in the near-Earth region. A simple explanation for this low ratio of Q/S in MBAs is that the survey of small MBAs is incomplete, many of Q-type MBAs might be discovered if the observations are able to detect the sub-kilometer-sized MBAs.

The collisional formation model of Q-type NEAs (hereafter, “standard model”) could be challenged by the rapid process of space weathering effect with solar wind implantation (Hapke, 2001; Vernazza et al., 2009), which timescale could be as short as $\sim 10^4$ to 10^6 years. Two arguments have been presented. First, kilometer-sized or large asteroids with collisional lifetimes exceeding 10^8 years (Bottke et al., 1993, 1994) should not display Q-type spectra under long-term space weathering effect. However, the existence of kilometer-sized Q-type NEAs, such as (1862) Apollo (Stuart and Binzel, 2004), contradicts the prediction of the “standard model”. Second, the high collisional rate in the main-belt region can produce asteroids with fresh surfaces more efficiently. On the other hand, the time scale of transport processes, such as the Yarkovsky effect and small resonances, that insert collisional fragments into the planet-crossing space also exceeds 10^6 years (Rabinowitz, 1997; Morbidelli and Vokrouhlický, 2003; Migliorini et al., 1998; Bottke et al., 2002; Binzel et al., 2004). Therefore, Q-type NEAs should not be present if they were primarily transferred from the main-belt with a Q-type spectra. This contradicts the observations made in near-Earth space.

An alternative scenario involves a possibility that the surfaces of Q-type NEAs have been reset during planetary encounters, from which the surface materials were removed (Nesvorný et al., 2005) or re-arranged (Binzel et al., 2010) by tidal effect. This hypothesis has been tested by several theoretical and observational studies. For example, Marchi et al. (2006) determined that the spectral slope of Q-type asteroids is correlated with planet-crossing

frequency. Binzel et al. (2010) and Nesvorný et al. (2010) suggested that the Q-type NEAs have experienced encounters with the Earth, Venus and then the tidal forces from these terrestrial planets could refresh the asteroidal surfaces. DeMeo et al. (2014) proposed the possibility that this mechanism might also be valid for Mars. As a corollary, the planetary encounter models predicts that Q-type asteroids are rare among MBAs because of the low planetary encounter rate in the main-belt.

Nevertheless, the timescale of space weathering on asteroid surface is still in debate. Willman and Jedicke (2011) studied 95 asteroids for which span a size and age range of about 1-20 km and 100-3000 Myr, respectively, and measured a space weathering time of 2×10^9 years. This is much longer than the result of fast space weathering (Hapke, 2001; Vernazza et al., 2009). Polishook et al. (2014) also detected a Q-type asteroid in main-belt with age $\sim 10^6$ years indicating that the space weathering timescale should be no less than $\sim 10^6$ years.

The other mechanisms to create Q-type asteroids are correlated with fast rotation and YORP effect: 1. rotational-fission results in the exposure of material from the covered surface of parent asteroid (Polishook et al., 2014), and 2. rotational re-arrangement of asteroid surface material via landslips (Scheeres, 2015; Walsh et al., 2012) and partial removal of weathered regolith. These two mechanisms are able to uncover non-weathered materials and display the fresh Q-type spectra. Since the rotation of the smaller asteroids are easier to be accelerated by YORP effect, we expect to detect more small size Q-type MBAs if rotational effects are the dominant mechanism of the Q-type asteroid formation.

Delbo et al. (2014) reported recently that thermal degradation induced by diurnal temperature variation is able to break up rocks on the asteroid surface rapidly into new regolith layer. They also suggested that asteroids with large diurnal temperature difference (i.e., NEAs) can be cover by fresh regolith characterized by the Q-type spectra. This scenario predicts that more Q-type asteroids should be detected in near Earth space than in main-belt because of the larger diurnal temperature variation of NEAs. Note that the regolith formation by thermal fragmentation does not depend on asteroid size; it may also imply that there is no color-size relation in the NEA population.

From the discussion above, the multicolor observation of kilometer to sub-kilometer diameter MBAs becomes critical to understand the space weathering on S-complex asteroid surface and the formation of Q-type asteroids.

We should detect a comparable or even higher fraction of Q-type asteroids in the main-belt than the near-Earth region, if the space weathering timescale is $> 10^8$ years, and the collisional “standard model” dominate the formation of Q-type asteroids. By contrast, if the Q-type asteroid fraction in the main-belt is very low, the Q-type NEAs must form in-situ and other mechanism like the planetary encounter models, rotational-fission/re-arrangement or thermal degradation should be responsible of the formation of Q-type NEAs.

2. Observations and Data Reduction

To find sub-kilometer asteroids in the main-belt, we used the data taken by Subaru telescope with Suprime-Cam, which is a prime focus camera with a wide field of view ($34' \times 27'$) that consists of 10 CCD chips (Miyazaki et al., 2002). The observational dates were August 9 and 10, 2004 (UT).

Three fields were surveyed each night for approximately 3.5 hours from the midnight of Hawaii. The seeing size was 0.54-0.70 arcsecond on the first night and 0.77-1.06 arcsecond on the second night. The observational fields were near opposition and close to the ecliptic plane. The center of the coordinates of each observed field is listed in Table 1.

The images were obtained using four broadband filters: B , V , R and I . The exposure times were 120 sec for the B -, V - and R -bands and 180 sec for the I -band. The observations followed the color sequence $RR-BB-VV-RR-II-RR$ for each fields. The time interval of the first R -band set and the second R -band set was approximately 80 min. The interval between the second R -band set and the third R -band set was approximately 60 min. We used this three sets of R -band observations to interpolate the R magnitude in the epoch of B , V and I -band observations to avoid possible color uncertainty due to the asteroid rotational effect. Detailed description of photometric calibration can be found in Sections 2.2 and 2.3 in detail.

Table 1 Coordinates of the surveyed fields
Aug. 09, 2004

Field ID	RA	DEC	λ	β
F1-1	21:18:24	-15:11:00	317.306	0.488
F2-1	21:18:24	-15:41:00	317.154	0.011
F3-1	21:18:24	-16:11:00	317.003	-0.465

Aug. 10, 2004

Field ID	RA	DEC	λ	β
F1-2	21:22:12	-14:54:00	318.266	0.478
F2-2	21:22:12	-15:24:00	318.112	0.002
F3-2	21:22:12	-15:54:00	317.959	-0.474

2.1. Detection of Moving Objects

To detect moving objects in relatively crowded fields, we first stacked all 12 exposures in each field to obtain deep images. We then used these deep images as the source images to generate the reference stationary catalogs and remove all stationary sources in every exposure.

After removing the stationary sources, we used the KDTree-based nearest neighborhood search method to identify the detection pairs in every two consecutive exposures. The pairs detected in the first set of consecutive exposures were used to determine the main vectors for predicting the possible locations in the other five exposure pairs. We then searched for the corresponding pairs at the predicted locations of the other set of consecutive exposure. Once the entire set of six pairs (i.e., 12 detections in total) was identified, the complete set was passed to the *Orbfit* code (Bernstein and Khushalani, 2000) to ensure that the orbital solution are reasonable; the semi-major axis was between 2 AU and 5 AU, and the fitting residual was smaller than 0.5". Under these stringent conditions, all moving objects detected are real and complete color measurements were performed for all of them. The asteroid detection list is summarized in Table 2.

Table 2. Asteroid list

RA (°)	DEC (°)	Epoch (MJD)	a (AU) ^a	i (°) ^a	H _V	B	B _{err}	V	V _{err}	R	R _{err}	I	I _{err}	A ^b	A _{err} ^b	Comment	a (AU) ^c	e ^c	i (°) ^c
319.48272	-15.40419	53226.529043	2.84	2.31	18.103	22.561	0.014	21.690	0.002	21.277	0.011	20.926	0.008	0.088	0.011				
319.39225	-15.22197	53226.529043	2.90	4.69	19.612	24.146	0.021	23.320	0.002	22.981	0.017	22.584	0.001	0.004	0.106				
319.69678	-15.20883	53226.529043	3.21	0.03	18.980	23.970	0.025	23.231	0.037	22.980	0.038	22.661	0.001	-0.119	0.053				
319.46102	-15.20154	53226.529043	3.09	16.65	19.088	23.911	0.008	23.141	0.003	22.749	0.017	22.246	0.016	0.002	0.034				
319.46236	-15.19466	53226.529043	2.25	5.50	18.683	21.583	0.030	20.930	0.012	20.607	0.014	20.563	0.027	-0.130	0.024				
319.58996	-15.18535	53226.529043	2.55	8.45	19.353	23.149	0.001	22.336	0.026	21.922	0.013	21.560	0.012	0.048	0.048				
319.57579	-15.16933	53226.529043	2.84	9.71	18.900	23.027	0.012	22.493	0.006	21.859	0.012	21.519	0.023	0.006	0.020				
319.38260	-15.16018	53226.529043	3.05	0.16	19.211	23.882	0.087	23.200	0.015	23.056	0.032	22.667	0.020	-0.236	0.140				
319.34533	-15.16815	53226.529043	2.56	23.00	21.014	25.138	0.016	24.025	0.023	23.339	0.240	22.887	0.050	0.452	0.351				
319.63049	-15.14830	53226.529043	2.92	1.07	20.022	24.513	0.255	23.774	0.046	23.602	0.048	23.087	0.125	-0.176	0.245				
319.86432	-15.11508	53226.529043	2.53	11.95	15.351	19.177	0.002	18.279	0.003	17.823	0.003	17.423	0.009	0.138	0.003				
319.37775	-15.09740	53226.529043	2.85	2.08	19.851	24.105	0.030	23.461	0.012	23.022	0.064	22.618	0.041	-0.054	0.050				
319.82910	-15.09154	53226.529043	3.46	0.68	18.449	23.810	0.041	23.106	0.028	22.772	0.037	22.467	0.009	-0.086	0.044				
319.58372	-15.09950	53226.529043	2.61	19.12	18.133	22.075	0.010	21.258	0.003	20.762	0.013	20.367	0.004	0.109	0.008				
319.81048	-15.08243	53226.529043	2.99	13.25	19.227	23.837	0.042	23.096	0.028	22.738	0.049	22.321	0.026	-0.042	0.040				
319.72990	-15.05428	53226.529043	2.91	0.46	19.240	23.795	0.052	22.967	0.004	22.727	0.051	22.365	0.019	-0.065	0.104				
319.31365	-15.03409	53226.529043	2.71	7.15	19.777	23.905	0.011	23.108	0.006	22.726	0.015	22.375	0.057	0.014	0.045				
319.86975	-15.03411	53226.529043	2.91	4.80	15.174	19.783	0.008	18.904	0.000	18.410	0.003	17.941	0.002	0.151	0.008				
319.32668	-15.01941	53226.529043	2.92	1.91	17.177	21.680	0.006	20.918	0.002	20.463	0.007	20.018	0.020	0.041	0.006				
319.70512	-14.98392	53226.529043	2.29	5.76	19.579	22.853	0.033	21.928	0.013	21.657	0.003	21.035	0.024	0.025	0.031				
319.76720	-15.30467	53226.529043	3.28	10.14	17.388	22.444	0.001	21.760	0.002	21.409	0.008	21.071	0.003	-0.089	0.027				
319.88038	-15.29547	53226.529043	2.41	2.13	19.033	22.554	0.020	21.687	0.012	21.228	0.008	20.831	0.008	0.118	0.019				
319.74818	-15.28862	53226.529043	2.68	4.36	15.391	19.505	0.001	18.654	0.003	18.189	0.001	17.780	0.020	0.111	0.003	(62523) 2000 SW24	2.7	0.07	4.28
319.30847	-15.28169	53226.529043	3.16	10.69	18.476	23.424	0.028	22.650	0.021	22.377	0.022	21.998	0.011	-0.080	0.041				
319.86194	-15.28194	53226.529043	2.97	8.94	19.373	23.631	0.085	23.205	0.163	22.552	0.029	22.227	0.050	-0.057	0.208				
319.71990	-15.27244	53226.529043	3.03	14.48	20.092	25.335	0.035	24.039	0.074	23.739	0.039	23.551	0.052	0.308	0.075				
319.35283	-15.27298	53226.529043	2.72	4.47	20.254	24.188	0.004	23.599	0.053	23.245	0.020	22.988	0.002	-0.153	0.064				
319.83410	-15.23152	53226.529043	3.01	9.89	17.812	22.470	0.004	21.713	0.015	21.393	0.016	21.670	0.434	-0.058	0.025				
319.62572	-15.22084	53226.529043	2.91	1.49	13.441	17.950	0.005	17.165	0.011	16.909	0.039	16.808	0.028	-0.084	0.018				
319.69906	-15.22543	53226.529043	3.06	0.96	19.460	24.116	0.056	23.453	0.063	23.019	0.036	22.602	0.004	-0.045	0.067				
320.70343	-15.12162	53227.533671	2.54	0.60	19.229	23.109	0.009	22.184	0.009	21.719	0.019	21.398	0.002	0.163	0.035				
320.65551	-15.05483	53227.533671	2.99	1.51	16.549	21.252	0.001	20.414	0.004	19.955	0.004	19.528	0.005	0.097	0.004				
320.68576	-15.01347	53227.533671	2.88	3.55	18.366	22.788	0.006	22.040	0.021	21.655	0.020	21.333	0.004	-0.019	0.016				

Table 2 (cont'd)

	RA (°)	DEC (°)	Epoch (MJD)	a (AU) ^a	i (°) ^a	H _V	B	B _{err}	V	V _{err}	R	R _{err}	I	I _{err}	A ^b	A _{err} ^b	Comment	a (AU) ^c	e ^c	i (°) ^c
∞	320.59647	-15.00993	53227.533671	3.03	10.02	19.492	24.327	0.030	23.437	0.034	23.172	0.025	22.874	0.016	-0.003	0.047	(252718) 2002 CQ194	3.01	0.08	3.47
	320.33657	-14.97422	53227.533671	3.04	2.47	17.160	22.045	0.004	21.123	0.012	20.678	0.007	20.248	0.002	0.146	0.015				
	320.66292	-14.89674	53227.533671	3.05	0.55	19.167	24.113	0.025	23.148	0.110	22.830	0.077	22.386	0.042	0.087	0.092				
	320.44262	-14.85440	53227.533671	2.64	3.27	19.728	24.209	0.063	22.907	0.191	22.512	0.049	22.306	0.037	0.380	0.220	Q-type candidate			
	320.58374	-14.84279	53227.533671	3.12	0.43	16.584	21.393	0.009	20.680	0.009	20.331	0.005	19.975	0.001	-0.069	0.016				
	320.26807	-14.82940	53227.533671	2.88	2.04	16.242	20.761	0.006	19.912	0.001	19.504	0.005	19.183	0.003	0.069	0.015				
	320.54242	-14.80967	53227.533671	2.94	9.75	19.503	23.711	0.160	23.289	0.049	22.955	0.029	22.512	0.023	-0.285	0.152				
	320.52186	-14.78980	53227.533671	3.11	2.37	18.405	23.366	0.013	22.495	0.016	21.906	0.078	21.411	0.022	0.213	0.031				
	319.51576	-15.68548	53226.534619	2.50	9.54	20.173	23.905	0.032	23.036	0.001	22.675	0.011	22.290	0.010	0.050	0.033				
	319.85629	-15.67499	53226.534619	2.57	6.24	20.294	24.496	0.009	23.330	0.062	23.168	0.013	22.646	0.090	0.119	0.062				
	319.75825	-15.67583	53226.534619	2.31	0.80	21.302	24.414	0.004	23.709	0.069	23.215	0.022	22.703	0.048	0.028	0.108				
	319.67486	-15.66787	53226.534619	2.14	1.03	22.288	24.940	0.189	24.237	0.004	23.481	0.063	23.408	0.000	0.212	0.158				
	319.67821	-15.66154	53226.534619	3.23	2.79	19.251	23.904	0.309	23.531	0.024	23.224	0.036	22.888	0.035	-0.339	0.221				
	319.38817	-15.64510	53226.534619	2.68	8.59	20.630	24.276	0.162	23.901	0.102	23.324	0.039	23.055	0.008	-0.146	0.141				
	319.50101	-15.63361	53226.534619	2.41	3.41	14.861	18.618	0.007	17.524	0.012	17.207	0.014	16.954	0.012	0.178	0.013	(204290) 2004 PV21	2.17	0.1	6.36
	319.70150	-15.63029	53226.534619	2.19	7.19	16.856	19.749	0.004	18.932	0.003	18.346	0.043	18.092	0.003	0.172	0.005				
	319.72054	-15.60861	53226.534619	2.60	3.43	17.202	21.007	0.002	20.289	0.006	19.983	0.006	19.638	0.000	-0.095	0.005				
	319.36405	-15.57624	53226.534619	2.92	7.74	18.437	22.750	0.010	22.180	0.111	21.635	0.008	21.247	0.008	-0.031	0.106				
	319.30469	-15.51043	53226.534619	2.93	1.91	19.062	23.533	0.026	22.831	0.012	22.508	0.013	22.208	0.022	-0.095	0.063				
	319.30965	-15.50791	53226.534619	2.52	3.71	21.024	24.562	0.079	23.941	0.050	23.454	0.096	23.684	0.008	-0.037	0.143				
	319.36096	-15.50186	53226.534619	2.54	17.38	19.236	22.934	0.044	22.198	0.017	21.540	0.014	21.088	0.000	0.166	0.040				
	319.54940	-15.87029	53226.534619	2.43	6.49	19.608	23.105	0.043	22.312	0.003	21.859	0.025	21.406	0.009	0.062	0.034				
	319.35954	-15.87175	53226.534619	2.69	0.02	20.663	24.784	0.009	23.956	0.019	23.692	0.048	23.171	0.112	-0.048	0.022				
	319.60794	-15.85584	53226.534619	2.61	14.67	20.238	24.104	0.094	23.357	0.063	22.864	0.014	22.486	0.017	0.057	0.101				
	319.84755	-15.86667	53226.534619	3.00	13.01	18.785	23.621	0.263	22.670	0.008	22.254	0.023	21.901	0.009	0.147	0.187				
	319.80565	-15.84336	53226.534619	3.13	8.43	15.163	20.077	0.000	19.285	0.011	18.832	0.007	18.504	0.002	0.061	0.012				
	319.74746	-15.84407	53226.534619	2.65	0.94	19.940	23.945	0.002	23.142	0.029	22.692	0.020	22.297	0.038	0.066	0.027				
	319.49048	-15.83221	53226.534619	2.84	2.87	17.144	21.536	0.010	20.732	0.007	20.299	0.004	19.942	0.002	0.055	0.009				
	319.61032	-15.82195	53226.534619	2.64	2.77	20.579	24.493	0.038	23.763	0.031	23.312	0.033	22.931	0.013	0.015	0.060				
	319.46590	-15.82367	53226.534619	3.11	1.35	17.336	21.778	0.003	21.417	0.001	20.367	0.399	20.501	0.008	0.177	0.009				
	319.70470	-15.80420	53226.534619	2.43	6.59	20.853	24.404	0.020	23.553	0.026	23.061	0.040	22.749	0.013	0.130	0.029				
	319.47202	-15.79704	53226.534619	2.77	5.62	20.608	24.561	0.061	24.058	0.024	23.762	0.068	23.680	0.044	-0.255	0.061				
	319.59842	-15.79135	53226.534619	2.77	3.68	19.621	23.884	0.015	23.078	0.008	22.683	0.032	22.294	0.047	0.030	0.048				

Table 2 (cont'd)

RA (°)	DEC (°)	Epoch (MJD)	a (AU) ^a	i (°) ^a	H _V	B	B _{err}	V	V _{err}	R	R _{err}	I	I _{err}	A ^b	A _{err} ^b	Comment	a (AU) ^c	e ^c	i (°) ^c
319.61758	-15.79291	53226.534619	2.23	4.60	20.205	22.574	0.211	22.403	0.213	21.716	0.010	21.393	0.017	-0.213	0.232				
319.45546	-15.78328	53226.534619	2.49	4.66	17.988	21.554	0.000	20.831	0.004	20.460	0.005	20.094	0.001	-0.047	0.005				
319.75107	-15.77375	53226.534619	2.71	3.71	20.252	24.560	0.019	23.586	0.039	23.325	0.037	22.823	0.042	0.053	0.048				
319.71019	-15.75217	53226.534619	2.47	1.68	19.898	23.581	0.031	22.691	0.014	22.219	0.011	21.775	0.044	0.143	0.042				
319.39739	-15.74895	53226.534619	2.77	6.53	18.324	22.572	0.030	21.779	0.007	21.291	0.007	20.898	0.001	0.086	0.022				
319.43563	-15.73506	53226.534619	2.64	1.59	20.248	24.317	0.005	23.435	0.014	23.026	0.017	22.388	0.156	0.093	0.037				
319.35384	-15.72188	53226.534619	2.80	5.80	18.519	22.810	0.017	22.026	0.005	21.627	0.028	21.333	0.010	0.017	0.013				
320.42609	-15.57531	53227.539246	2.22	3.42	15.012	17.950	0.005	17.171	0.005	16.604	0.007	16.435	0.037	0.132	0.008	(6919) Tomonaga	2.26	0.1	5.16
320.79772	-15.55019	53227.539246	2.72	4.30	18.238	22.254	0.019	21.593	0.014	21.240	0.014	20.890	0.024	-0.103	0.024				
320.71232	-15.53839	53227.539246	3.04	2.51	18.195	22.782	0.007	22.164	0.023	21.677	0.063	21.371	0.003	-0.039	0.029				
320.82430	-15.53347	53227.539246	2.54	3.91	19.103	22.670	0.042	22.071	0.034	21.274	0.062	20.832	0.022	0.167	0.085				
320.32744	-15.53627	53227.539246	2.28	3.97	17.616	20.842	0.008	19.942	0.017	19.459	0.004	19.066	0.003	0.158	0.014				
320.33516	-15.52610	53227.539246	2.38	3.91	18.111	21.565	0.002	20.702	0.018	20.258	0.005	19.823	0.014	0.104	0.013				
320.67588	-15.49924	53227.539246	3.16	10.05	18.341	23.253	0.030	22.519	0.004	22.227	0.004	21.915	0.009	-0.094	0.034				
320.41969	-15.47944	53227.539246	2.37	7.19	20.047	23.933	0.117	22.608	0.009	22.424	0.060	22.051	0.018	0.247	0.091				
320.58908	-15.46737	53227.539246	3.30	4.38	15.615	20.736	0.013	20.020	0.001	19.653	0.023	19.338	0.013	-0.054	0.009				
320.28343	-15.45079	53227.539246	2.72	5.32	17.285	21.499	0.001	20.642	0.010	20.278	0.007	19.797	0.055	0.043	0.010				
320.80845	-15.38456	53227.539246	3.00	7.79	15.556	20.261	0.008	19.456	0.002	19.141	0.005	18.844	0.005	-0.028	0.006				
320.49664	-15.38502	53227.539246	2.89	2.26	19.593	24.077	0.132	23.271	0.006	22.923	0.216	22.194	0.003	-0.004	0.099				
320.63919	-15.37706	53227.539246	3.30	14.74	17.682	23.284	0.057	22.088	0.092	22.118	0.010	21.781	0.005	0.004	0.090				
320.63703	-15.38200	53227.539246	2.57	10.28	18.101	22.082	0.130	21.137	0.001	20.780	0.011	20.310	0.012	0.100	0.093				
320.54423	-15.37073	53227.539246	2.68	6.37	19.424	23.435	0.044	22.698	0.013	22.313	0.014	21.963	0.012	-0.027	0.083				
320.32559	-15.33817	53227.539246	3.05	1.41	17.527	22.273	0.004	21.516	0.019	21.192	0.005	20.675	0.000	-0.055	0.014				
320.76977	-15.30567	53227.539246	3.02	0.90	17.848	22.515	0.017	21.767	0.024	21.427	0.007	21.112	0.009	-0.051	0.024				
320.70791	-15.28156	53227.539246	2.34	1.87	18.318	21.534	0.002	20.805	0.001	20.412	0.006	20.038	0.007	-0.027	0.005	(2014) AR8	2.4	0.14	1.72
320.45096	-15.27708	53227.539246	2.24	1.83	17.172	20.377	0.005	19.389	0.008	18.891	0.010	18.554	0.021	0.231	0.009	(151733) 2003 BA88	2.32	0.15	2.64
320.64892	-15.22799	53227.539246	2.45	2.77	19.498	23.051	0.010	22.241	0.035	21.872	0.023	21.580	0.041	0.014	0.030				
320.63783	-15.20756	53227.539246	2.72	0.08	18.807	22.916	0.029	22.153	0.025	21.774	0.014	21.434	0.021	-0.012	0.037				
319.35421	-16.19792	53226.540177	3.11	0.65	18.054	22.743	0.020	22.135	0.010	21.703	0.009	21.590	0.001	-0.084	0.024				
319.60419	-16.39941	53226.540177	2.42	4.00	20.306	23.827	0.051	22.981	0.184	22.668	0.397	22.918	0.070	0.000	0.173				
319.34255	-16.38858	53226.540177	3.78	13.11	17.136	23.051	0.021	22.249	0.008	21.799	0.021	21.476	0.024	0.065	0.021	Q-type candidate			
319.62069	-16.37934	53226.540177	2.82	9.67	18.962	23.206	0.054	22.507	0.026	22.084	0.015	21.272	0.299	-0.027	0.047				
319.33731	-16.17518	53226.540177	2.84	2.81	20.090	24.511	0.038	23.689	0.048	23.318	0.080	23.047	0.076	0.024	0.098				

Table 2 (cont'd)

RA (°)	DEC (°)	Epoch (MJD)	a (AU) ^a	i (°) ^a	H _V	B	B _{err}	V	V _{err}	R	R _{err}	I	I _{err}	A ^b	A _{err} ^b	Comment	a (AU) ^c	e ^c	i (°) ^c
319.57251	-16.37746	53226.540177	2.62	2.94	18.422	22.469	0.004	21.555	0.006	21.091	0.008	20.694	0.008	0.155	0.015				
319.86114	-16.36801	53226.540177	2.35	1.14	20.808	24.117	0.028	23.307	0.025	22.627	0.025	22.147	0.018	0.234	0.047				
319.64018	-16.13018	53226.540177	2.98	12.47	18.580	23.257	0.085	22.428	0.008	22.049	0.007	21.657	0.002	0.035	0.061				
319.54882	-16.12899	53226.540177	2.77	6.70	19.475	23.585	0.022	22.919	0.019	22.515	0.041	22.737	0.081	-0.064	0.036				
319.32721	-16.11899	53226.540177	2.95	15.29	16.878	21.484	0.003	20.680	0.007	20.161	0.011	19.713	0.002	0.115	0.014				
319.60643	-16.12420	53226.540177	2.59	3.05	18.688	22.621	0.009	21.759	0.003	21.339	0.008	20.964	0.009	0.087	0.014				
319.82640	-16.10238	53226.540177	2.59	3.40	20.109	23.909	0.049	23.185	0.051	22.704	0.034	22.295	0.010	0.032	0.064				
319.51692	-16.09192	53226.540177	3.02	7.10	18.453	23.231	0.004	22.387	0.012	21.858	0.017	21.456	0.011	0.150	0.025				
319.83680	-16.07527	53226.540177	2.35	2.16	19.252	22.467	0.011	21.753	0.005	21.402	0.014	21.058	0.002	-0.067	0.011				
319.76208	-16.06889	53226.540177	2.96	11.26	18.247	22.939	0.010	22.072	0.096	21.766	0.015	21.404	0.007	0.009	0.103				
319.72250	-16.06501	53226.540177	2.67	7.38	18.203	22.303	0.007	21.451	0.013	21.008	0.007	20.626	0.008	0.096	0.019				
319.36741	-16.05471	53226.540177	3.06	7.98	18.246	23.006	0.009	22.250	0.034	21.893	0.009	21.517	0.008	-0.033	0.067				
319.47395	-16.04208	53226.540177	3.07	8.63	19.673	24.456	0.005	23.684	0.012	23.343	0.016	22.974	0.008	-0.033	0.055				
319.85396	-16.35700	53226.540177	2.91	1.61	18.683	23.172	0.046	22.411	0.039	22.125	0.032	21.742	0.005	-0.080	0.046				
319.72944	-16.02779	53226.540177	2.52	6.36	19.079	22.897	0.021	22.000	0.007	21.660	0.026	21.253	0.010	0.055	0.024				
319.73087	-16.35587	53226.540177	2.75	1.16	16.955	21.061	0.009	20.376	0.012	19.827	0.005	19.377	0.020	0.052	0.014				
319.76130	-16.02214	53226.540177	2.68	1.49	20.524	24.626	0.030	23.783	0.031	23.335	0.025	23.170	0.004	0.093	0.108				
319.58537	-16.01515	53226.540177	2.65	1.79	20.121	24.249	0.022	23.332	0.076	22.790	0.057	22.347	0.099	0.212	0.083				
319.61491	-16.00706	53226.540177	2.75	4.22	19.611	23.959	0.006	23.030	0.025	22.592	0.022	22.195	0.011	0.147	0.021				
319.43173	-16.00280	53226.540177	3.02	0.46	13.083	17.621	0.007	17.015	0.005	16.939	0.030	16.792	0.008	-0.338	0.007				
319.72263	-16.35138	53226.540177	2.98	5.89	19.868	24.295	0.106	23.729	0.042	23.196	0.029	22.892	0.087	-0.043	0.107				
319.62979	-15.96643	53226.540177	2.81	2.03	17.485	21.699	0.010	21.014	0.007	20.651	0.617	20.661	0.320	-0.079	0.014				
319.51548	-15.97303	53226.540177	2.39	6.87	17.151	20.531	0.005	19.769	0.002	19.490	0.010	19.097	0.002	-0.083	0.004				
319.69070	-15.97569	53226.540177	3.02	9.71	14.657	19.295	0.004	18.576	0.005	18.222	0.006	17.868	0.002	-0.061	0.005				
319.45615	-16.33313	53226.540177	2.99	12.99	18.454	23.144	0.004	22.319	0.009	21.933	0.025	21.498	0.031	0.036	0.015				
319.69838	-16.32601	53226.540177	2.51	0.48	20.177	24.522	0.018	23.069	0.406	23.014	0.050	22.693	0.037	0.247	0.303				
319.69109	-16.28867	53226.540177	2.63	6.04	20.354	23.898	0.198	23.519	0.050	23.163	0.021	22.787	0.005	-0.300	0.147				
319.85657	-16.27948	53226.540177	3.12	0.50	19.148	23.844	0.026	23.243	0.003	22.847	0.027	22.483	0.043	-0.115	0.024				
319.85490	-16.26903	53226.540177	2.68	2.55	20.756	24.994	0.056	24.023	0.117	23.626	0.089	23.131	0.099	0.147	0.167				
319.56316	-16.23162	53226.540177	3.22	4.24	15.270	20.221	0.006	19.547	0.020	19.088	0.012	18.382	0.013	-0.019	0.021				
319.42440	-16.20991	53226.540177	2.96	0.96	20.773	25.443	0.034	24.592	0.056	24.029	0.040	23.412	0.061	0.179	0.079				
320.79963	-16.11936	53227.544813	2.99	1.87	18.126	22.710	0.008	21.997	0.018	21.638	0.034	21.361	0.009	-0.062	0.041				
320.56040	-16.08520	53227.544813	2.04	5.53	21.185	23.541	0.010	22.824	0.023	22.194	0.017	21.742	0.022	0.132	0.024				

2.2. Flux Calibration

The Suprime-Cam image data were calibrated chip by chip in every exposure by identifying Pan-STARRS 1 (hereafter PS1) catalogue stars in the observed field; the data were calibrated using “uber-calibration” (Magnier et al., 2013). Uber-calibration is an algorithm used to photometrically calibrate wide-field optical imaging surveys, and it was first applied to the Sloan Digital Sky Survey imaging data. It can be used to simultaneously solve for the calibration parameters and relative stellar fluxes through the use of overlapping observations (Padmanabhan et al., 2008). Those uber-calibrated catalogues have a relative precision (compared with the SDSS) of < 10 mmag in g_{P1} , r_{P1} , and i_{P1} , and approximately 10 mmag in z_{P1} and y_{P1} (Schlafly et al., 2012). Since we used the B , V , R , I filters in our survey, we transferred those PS1 catalogue stars from the PS1 $g_{P1}r_{P1}i_{P1}$ photometry system to our Johnson-Cousins $BVRI$ system by using the transformation equation and parameters obtained by Tonry et al. (2012). The transformation error was approximately 0.03 in the B -band and 0.01 to 0.02 in the V -, R -, I -bands.

2.3. Trail Fitting

Two problems occur when using the traditional photometry methods for asteroid flux measurements: First, the flux would be contaminated by nearby stars if aperture photometry is used to measure the asteroid flux within crowded fields. Second, PSF fitting fails to yield accurate results if the asteroid image is not point-source-like object under long exposure. Therefore, we applied the trail fitting technique to measure the asteroid flux.

The trail function chosen is an axisymmetric Gaussian PSF-convolution trail function given in equation (3) of Vereš et al. (2012):

$$g[x', y'] = b + \frac{F}{L} \frac{1}{2\sigma (2\pi)^{1/2}} \exp \left[-\frac{y'^2}{2\sigma^2} \right] \left\{ \operatorname{erf} \left[\frac{x' + \frac{1}{2}L}{\sigma\sqrt{2}} \right] - \operatorname{erf} \left[\frac{x' - \frac{1}{2}L}{\sigma\sqrt{2}} \right] \right\}, \quad (1)$$

where

$$\operatorname{erf}[z] = \frac{2}{\pi} \int_0^z \exp[-t^2] dt \quad (2)$$

and

$$x' = (x - x_c) \cos \theta + (y - y_c) \sin \theta, \quad (3)$$

$$y' = -(x - x_c) \sin \theta + (y - y_c) \cos \theta, \quad (4)$$

Table 2 (cont'd)

RA (°)	DEC (°)	Epoch (MJD)	a (AU) ^a	i (°) ^a	H _V	B	B _{err}	V	V _{err}	R	R _{err}	I	I _{err}	A ^b	A _{err} ^b	Comment	a (AU) ^c	e ^c	i (°) ^c
320.64800	-16.03000	53227.544813	2.87	17.42	17.010	21.444	0.009	20.651	0.006	20.265	0.005	19.901	0.006	0.014	0.009				
320.27458	-16.02996	53227.544813	3.05	7.99	17.404	22.289	0.046	21.376	0.014	20.940	0.011	20.564	0.024	0.134	0.035				
320.40652	-16.01986	53227.544813	2.29	12.74	20.260	23.424	0.047	22.600	0.020	22.209	0.028	21.855	0.002	0.039	0.047				
320.31635	-16.00107	53227.544813	2.25	0.53	19.489	22.591	0.019	21.726	0.000	21.300	0.008	20.938	0.004	0.093	0.026				
320.82385	-15.98608	53227.544813	2.44	3.24	18.920	22.623	0.021	21.652	0.010	21.032	0.009	20.621	0.007	0.305	0.021				
320.71048	-15.93982	53227.544813	2.64	4.53	19.094	23.258	0.031	22.283	0.004	21.818	0.010	21.453	0.019	0.198	0.028				
320.65166	-15.91541	53227.544813	2.33	7.10	20.093	23.306	0.004	22.550	0.007	22.065	0.029	21.109	0.511	0.057	0.006				
320.62216	-15.91270	53227.544813	3.13	3.21	16.622	21.451	0.007	20.738	0.007	20.321	0.004	19.957	0.001	-0.021	0.008				
320.39658	-15.87950	53227.544813	2.56	2.40	19.464	23.241	0.008	22.462	0.062	22.075	0.010	21.649	0.004	0.004	0.062				
320.41451	-15.86789	53227.544813	2.72	3.93	18.944	22.866	0.126	22.304	0.055	21.900	0.047	21.499	0.038	-0.137	0.119				
320.39999	-15.85829	53227.544813	3.10	0.75	18.993	23.920	0.041	23.057	0.044	22.648	0.020	22.590	0.149	0.079	0.048				
320.70450	-15.85786	53227.544813	2.64	1.98	19.097	23.084	0.035	22.283	0.010	21.895	0.013	21.556	0.000	0.021	0.040				
320.66966	-15.78510	53227.544813	3.22	1.12	15.826	20.814	0.018	20.095	0.006	19.707	0.004	19.393	0.004	-0.037	0.014				
320.65956	-15.74312	53227.544813	2.91	24.42	17.230	21.705	0.018	20.951	0.000	20.661	0.006	20.222	0.001	-0.082	0.015				
320.51081	-15.74918	53227.544813	2.69	6.83	19.273	23.438	0.014	22.559	0.000	22.276	0.032	21.796	0.000	0.002	0.018				
320.65568	-15.73321	53227.544813	2.51	3.04	19.194	23.230	0.011	22.099	0.010	21.434	0.127	21.270	0.001	0.450	0.027				
320.32995	-15.71095	53227.544813	3.08	12.77	18.356	23.137	0.015	22.386	0.037	22.007	0.007	21.630	0.004	-0.021	0.032				
320.30033	-15.68513	53227.544813	3.15	10.08	18.531	23.528	0.019	22.691	0.000	22.247	0.010	21.592	0.191	0.086	0.030				

Note. — ^a Estimated by using Equation 6, 7,8 and 9 under assuming e=0.

Note. — ^b See Equation 13.

Note. — ^c Orbital elements of known asteroids are provided by JPL Small-Body Database.

where b is the background level, L is the length of the trail, F is the total integrated flux in the trail, σ is the standard deviation of the PSF Gaussian, x_c and y_c are the coordinates of the centroid of the trail. θ is the angle between the long axis of the trail and the x axis.

We used the Levenberg-Marquardt least-squares fitting technique to minimize the variance between the image and trail function. Figure 1 shows an example of an asteroid trail and its fitting residue. Clearly, the asteroid trail can be completely subtracted by using the trail function. The photometric error of the asteroid flux was estimated from the flux difference between two consecutive exposures of the asteroid; we considered the flux difference to be closer to the actual uncertainty compared with the estimation derived from the fitting result. We expect that the SNR of trail fitting photometry decreases with $(2.35\sigma/(2.35\sigma + L))^{0.5}$. Thus the faster mover have larger photometry uncertainty. Fortunately, there is no systematic effect related to the trail length (See Vereš et al. (2012) for more detail), and the photometry results should be independent with the semi-major axis of asteroids.

2.4. Detection Efficiency and De-biasing

For testing the detection efficiency of moving objects in the observations, we planted 500 non-trailing artificial stars with a brightness between 22.5 to 25.5 magnitude in each CCD chip. The artificial objects were generated by *IRAF* task *DAOPHOT* by modeling the stars in each CCD chip in each exposure. The limiting magnitude also depends on the trailing rate of asteroids. Assuming that the moving rate of asteroids is about $0.01''/\text{s}$ in average. We expect that the trail length is around $1.2''$ in the 120s exposure. For the average $0.7''$ seeing size of our data, the SNR of the asteroid trail is roughly 60% of the non-trailing source with the same brightness. Therefore, we increased the detection threshold of artificial non-trailing stars to 5 sigma to simulate the limiting magnitude of 3 sigma asteroid detections.

We counted the number of detected artificial objects with a function of magnitude and plotted a diagram of magnitude vs. fractional detection as shown in Figure 2, and fitted a detection efficiency function, which was a function with double hyperbolic tangents (Petit et al., 2006), to the test result:

$$\eta(R) = \frac{A}{4} [1 - \tanh(\frac{R - R_c}{\Delta_1})] [1 - \tanh(\frac{R - R_c}{\Delta_2})] \quad (5)$$

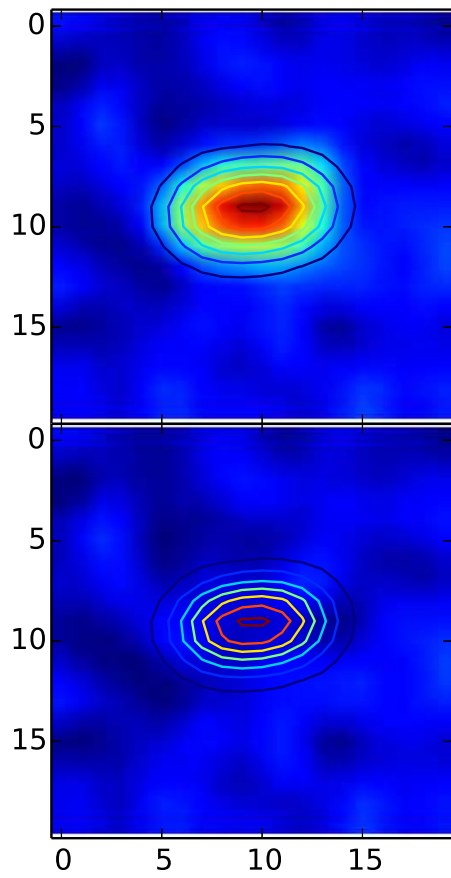


Figure 1 An example of an asteroid trail in our sample before (top) and after (bottom) subtracting its fitting result (contour).

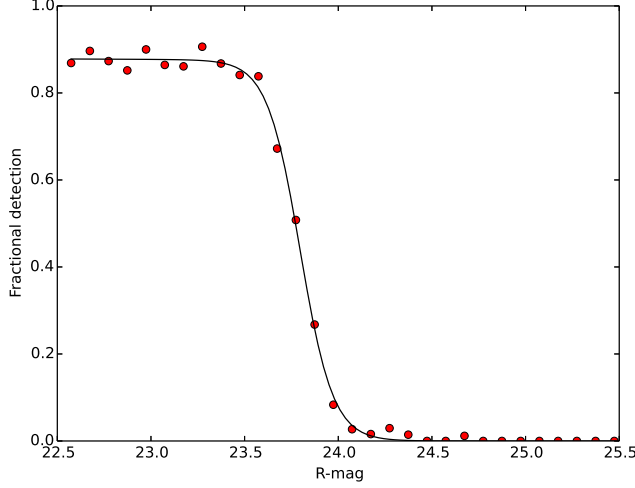


Figure 2 An example of fractional detection as a function of the R-magnitude. The best-fit detection efficiency function is illustrated.

Here, the fitted parameters A , R_c , Δ_1 and Δ_2 are the filling factor (or maximal efficiency), roll-over magnitude (50% of the maximal efficiency), and widths of the two components, respectively. An exemplary result for the R-band, Chip2, took on August 10, 2004 was the 50% detectability of approximately 23.7 magnitude, and the filling factor was approximately 83% (see Figure 2).

Using this detection efficiency function, we assigned a weight for each asteroid detection; the weight was the multiplicative inverse of the product of the detection efficiency of every chip and exposure of the asteroid that passed. The weight of the object with the highest detectability is 1, and fainter objects, which have a low detection probability, have a higher weighting value. Therefore, we eliminated the observational bias in the detection of objects and tested the completeness of the survey.

3. Results

3.1. Absolute Magnitude and Completeness

We extracted a total of 150 asteroids with 12 detections from the six fields and measured their apparent velocities. Assuming that their orbital

eccentricities were zero and they located around opposition during the observations, we estimated the semi-major axes and inclinations by using the following equations (Bowell and Lumme, 1979; Nakamura and Yoshida, 2002; Yoshida and Nakamura, 2007):

$$a = \frac{1}{2\gamma}(\gamma - 2k\lambda \pm \sqrt{|\kappa|}), \quad (6)$$

$$\tan I = \frac{|\beta|}{\lambda + k/(a - 1)}, \quad (7)$$

$$\gamma = \lambda^2 + \beta^2, \quad (8)$$

$$\kappa = \gamma^2 - 4k\lambda\gamma - 4k^2\beta^2, \quad (9)$$

where λ and β are the moving rate along the ecliptic longitude and latitude, respectively; a and I are the semi-major axis and inclinations, respectively; and k is the Gaussian gravitational constant. The semi-major axis and inclinations estimated using the aforementioned equations included errors of approximately 0.1 AU and 5° because the actual eccentricities of the asteroids were not zero. We compared the orbital elements of known asteroids in Table 2 with our estimated elements. The result shows that the estimate elements are generally accurate; the difference between known and estimated semi-major axes, inclinations are less than 0.1 AU, 2° , respectively.

The absolute magnitude (H_V) of each asteroid at opposition can be estimated using the following equation:

$$H_V = m - 5\log(\Delta r) \quad (10)$$

where m is the apparent magnitude of the asteroid and Δ and r are geocentric distance and heliocentric distance, respectively. For simplicity, $r = a$ and $\Delta = a - 1$ because of the $e = 0$ and nearly opposition assumptions.

Figure 3 shows the absolute magnitude (H_V) distribution of our samples. The black spikes are the raw H_V distribution, and the gray boxes shows the weighted result. Based on the results of Yoshida and Nakamura (2007), we plotted two power laws ($N(< H_V) \propto 10^{\alpha H_V}$) to the H_V distribution, with power law indices b of 1.29 (for the H_V range from 17.8 to 20.2 mag) and 1.75 (14.6 to 17.4 mag). Here $b = 5\alpha$. This plot clearly indicates that our samples have power law indices consist with the results of Yoshida and Nakamura (2007) and satisfactory completeness of up to $H_V = 20$, which corresponds to asteroids with diameters smaller than 590 meter for the C-complex asteroids

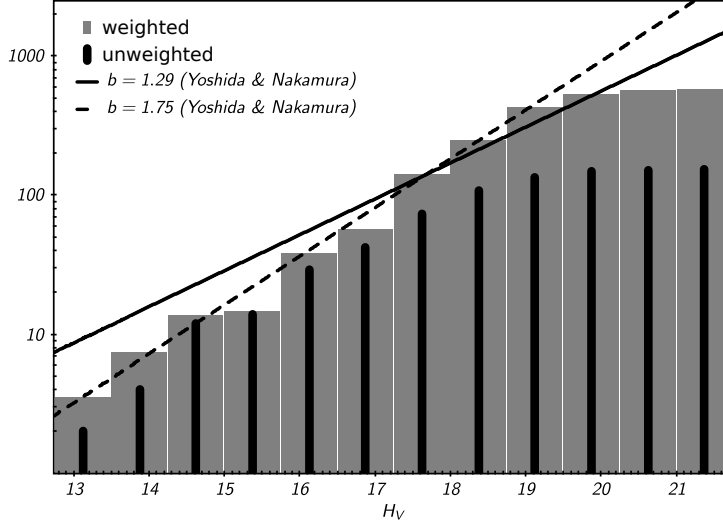


Figure 3 Weighted (Grey) and unweighted (black) cumulative absolute magnitude (H_V) distributions of the asteroids sample. Solid and dashed lines show the power laws distribution with power law indices of 1.29 (for the H_V range 17.8 to 20.2 mag) and 1.75 (14.6 to 17.4 mag), respectively.

(assuming an albedo of 0.05) and smaller than 270 meter for the S-complex asteroids (assuming an albedo of 0.25).

3.2. Colors and Estimated Taxonomic Types

From our sample (150 asteroids), 75 asteroids with the H_V range from 16 to 20 magnitude, the color errors smaller than 0.1, $0.2 < V - R < 0.6$ and $0.6 < B - V < 1$ was selected. These asteroids have satisfactory H_V completeness and photometric accuracy which made them suitable for taxonomic estimations. The color errors are propagated from the uncertainty of BVRI photometry of asteroids in Table 2. Figure 4 shows the relative reflectances in our asteroid samples overlap with the transmission curve of the Suprime-Cam filter system. The C-complex asteroids generally have a flat reflectance across the four filters, and the S-complex and V/Q/R-type asteroids exhibit similar slopes in the B, V, R region but different reflectances near the I-band; the V/Q/R-type asteroids demonstrated a stronger absorption feature at $\sim 1 \mu\text{m}$. Therefore, while $B - V$ and $V - R$ color are used to separate S-complex and C-complex asteroids, the $R - I$ color is needed to distinguish S-type asteroids from V/Q/R-type-like asteroids in the following sense. The

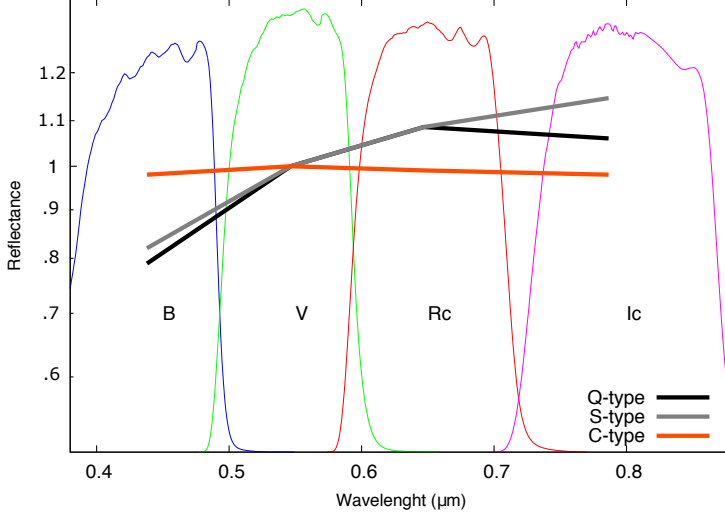


Figure 4 Spectrophotometry of three types of asteroid spectra: S-complex, C-complex and V/Q/R-type-like asteroids. The background shows the transmission curves of the Suprime-Cam filter system.

S-type asteroids are those with $R - I > (R - I)_{\odot}$ (0.332 ± 0.008 , according to Holmberg et al. (2006)); otherwise the V/Q/R-type-like asteroids.

We also separated our sample into large and small asteroids by $H_V = 18.5$, which approximately corresponds to a diameter of 1 km for C-complex asteroids. Figure 5 shows $B - V$ vs. $V - R$ color-color diagram for part of our large asteroid sample ($H_v < 18.5$). The bimodal distribution corresponds to the color difference between the C-complex and S-complex asteroids.

Moreover, we identified principal components (the uncorrelated variables) for the large asteroid sample in $B - V$ and $V - R$ space by principal component analysis to separate S-complex asteroids and C-complex asteroids and resulted two linear combinations of $B - V$ and $V - R$ colors:

$$PC1 \equiv 0.7071(B - V) + 0.7071(V - R), \quad (11)$$

and

$$PC2 \equiv 0.7071(B - V) - 0.7071(V - R) \quad (12)$$

The result shows that $B - V$ and $V - R$ axes become PC1 and PC2, respectively, after rotating 45° counterclockwise.

Furthermore, there is a dip at $PC1 = 0.82$ in the histogram of PC1 and can be the boundary of C and S-complex asteroids. Therefore, we define a

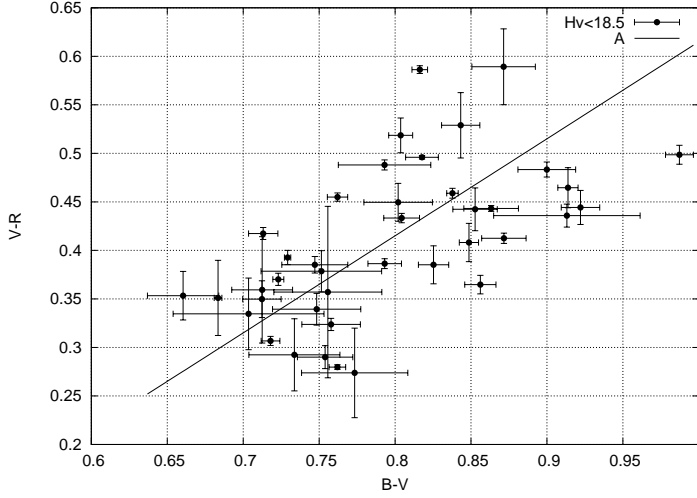


Figure 5 The $B - V$ and $V - R$ color-color diagram for our large asteroid sample ($H_V < 18.5$). The solid line shows the direction of new axis (A) of the color-color distribution.

new axis ‘A’:

$$A \equiv 0.7071(B - V) + 0.7071(V - R) - 0.82 \quad (13)$$

Asteroids with $A > 0$ should belong to S-complex, otherwise are C-complex. The new axis ‘A’ is shown as a solid line in Figure 5.

Figure 6 shows the color-color diagram of axis A vs. $R - I$. Each dot represents an asteroid. A value of 0.332, which is corresponding to the solar color, was subtracted from the $R - I$ axis to separate S-complex and V/Q/R-type. Two major points can be made based on Figure 6: (1) only two objects can be certified as Q-type MBA candidates; (2) the small sample ($H_V > 18.5$) appeared to be more concentrated at $A \approx 0$, though the C- and S-complexes are clearly separated in large sample ($H_V < 18.5$).

3.3. Fraction of Each Estimated Taxonomic Type

To estimate the taxonomic type of asteroids, we considered $A < 0$ as C-complex asteroids, $A > 0$ and $R - I - 0.332 > 0$ as S-complex and $A > 0$ and $R - I - 0.332 < 0$ as V/Q/R like asteroids. Four objects locate around D/T type region were removed by visually selection. Figure 7 shows the semi-major axis vs inclination distribution of the 75 asteroids with estimated

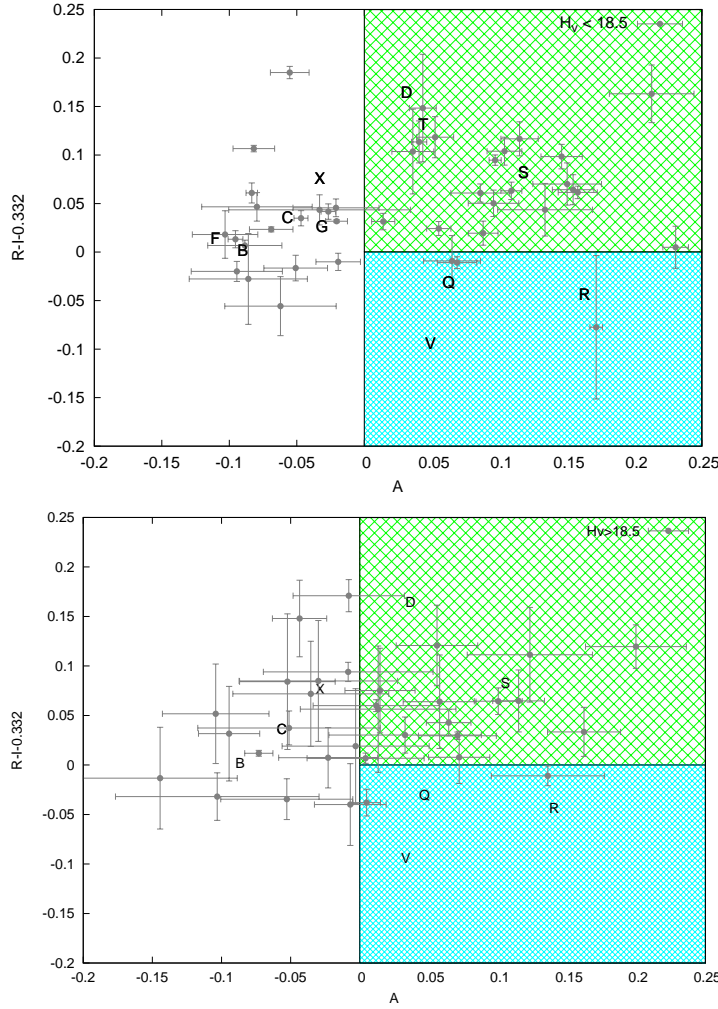


Figure 6 The $R - I$ vs. A color-color diagrams of the large (upper) and small (bottom) asteroid samples in the present Subaru data. The regions corresponding to three types of asteroids are shown in the plots. The average colors of B, C, D, F, G, S, T, V, Q, R and X-type asteroids from Dandy et al. (2003) are also marked.

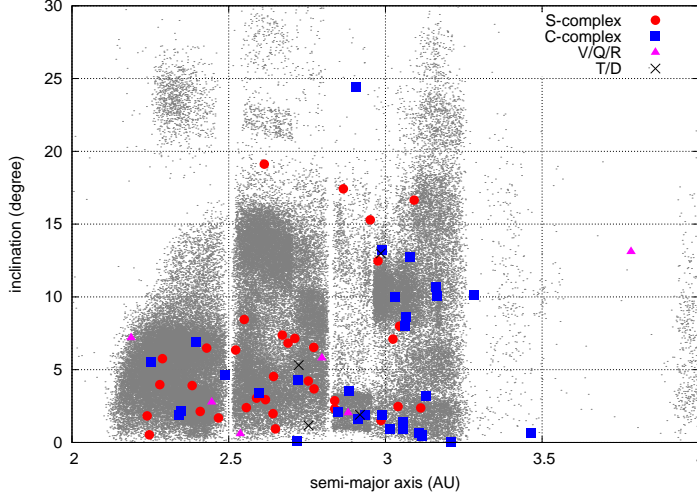


Figure 7 Semi-major axis (a) vs inclination (i) distribution of the 75 asteroids with estimated taxonomic type. Gray dots show the a, i distribution of known asteroids.

taxonomic type. The distribution looks normal; there are more C-complex than S-complex asteroids in outer main-belt. There is a possible V/Q/R-type candidate located on 3.8 AU. It could be because of wrong estimation in semi-major axis.

To calculate the fraction of each estimated taxonomic type, we took the uncertainty of boundaries of A and $R - I$ axes, which are 0.02 from the bin-size of A histogram and 0.008 from the uncertainty of $(R - I)_{\odot}$, respectively, and the uncertainty of asteroid color measurements into account. We use 2D gaussian distribution with a covariance matrix equal to

$$\begin{pmatrix} A_{err}^2 & 0 \\ 0 & (R - I)_{err}^2 \end{pmatrix}$$

to represent the probability distribution of each object in $A, R - I$ space. Therefore, the fraction of a object in a specific taxonomic type is its probability distribution multiply a Complementary Error Function, which is the cumulative function of a gaussian distribution with the mean value equal to boundary value and standard deviation equal to the uncertainty of boundary. Figure 8 shows the fraction of asteroid types in our weighted and unweighted sample.

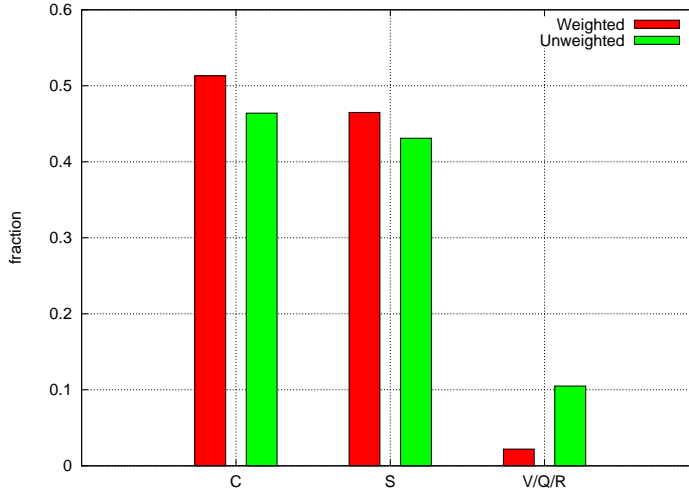


Figure 8 Histograms of the fractions of estimated asteroid spectral types. C and S are C-complex and S-complex asteroids, respectively, and V/Q/R indicates V/Q/R-type-like asteroids.

Since our sample exhibits a H_V range similar to that of the near-Earth asteroid sample used by Dandy et al. (2003), it is worth to compare the fraction of asteroid’s type to that of NEA population. The Q/S ratio in our observation is less than 0.05 in the main-belt region. By contrast, the Q/S ratio in the near earth space is about 0.5 (Binzel et al., 2004) to 2 (Dandy et al., 2003), which is much higher than in the main-belt.

Finally, we tested the correlation between H_V and $R - I$ of S-complex asteroids. As shown in Figure 9, unlike the result of Dandy et al. (2003) in which the absorption band depth was correlated with S-complex NEA size, we did not find any evidence that $R - I$ color has significant correlation with the size of S-complex MBA.

4. Discussion

There are only two possible Q-type asteroids candidates in our km to sub-km sized MBA sample (see Figure 6). This fact indicates that the Q-type asteroids are rare in the main-belt. The Q/S ratio is less than 0.05, which is significantly lower than the value of NEAs (~ 0.5 in Binzel et al. (2004) and ~ 2 in Dandy et al. (2003)). This result is also comparable with the

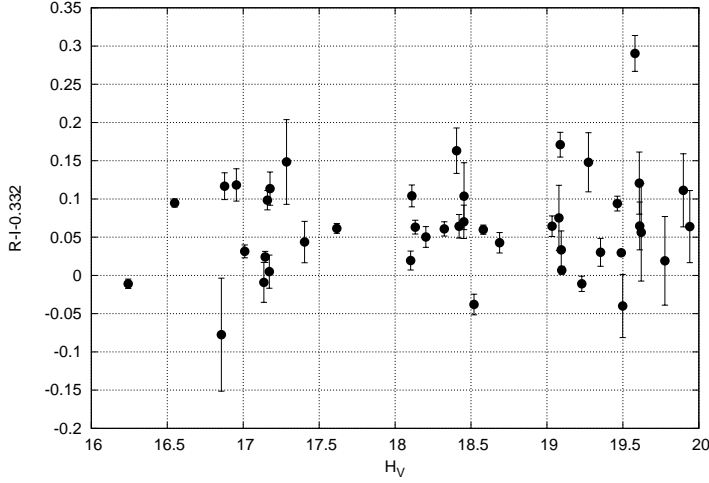


Figure 9 Variation of $R-I$ color (an indicator of absorption band depth) as a function of the absolute magnitude, H_v , for the observed S-complex MBAs.

Q-type-like fraction in Carvano et al. (2010), which the main belt Q/S ratio is $325/3784 \sim 0.09$ for the good classified asteroids in SDSSMOC4.

Since most of S-complex MBAs are weathered, we can estimate the upper limit of space weathering timescale in main belt by using the collisional size-age relation in Bottke et al. (2005) and Willman and Jedicke (2011):

$$T_s(\text{yr}) = 3.23 \times 10^{(11.0-0.18H_v)} \quad (14)$$

The H_v range of our MBA samples are between 16 to 20 magnitude, and their corresponding collisional ages are between 8×10^7 to 4×10^8 years. We can safely conclude that the space weathering timescale in main belt should be less than 10^8 years.

The lack of Q-type MBAs also suggests two facts: 1. Most of the Q-type NEAs did not come from main-belt, they must form in-situ, and 2. collision is not the main mechanism of the formation of Q-type NEAs due to the collision rate being lower in the near Earth region. There must exist other mechanisms to generate such large amount of Q-type NEAs, and these mechanisms are more effective in the near Earth region than the main-belt. The planetary encounter model (Binzel et al., 2010; Nesvorný et al., 2010) advocating the recent resetting of S-type asteroid surfaces by the effects of tidal stress is one of the possible mechanisms.

Another possible mechanism that could be responsible for the formation of Q-type NEAs is YORP effect spin-up induced rotational-fission or surface re-arrangement of asteroids. The acceleration rate of asteroid spin by the YORP effect is inversely proportional to the square of semi-major axis and more effective in the near Earth region than in the main-belt due to the smaller heliocentric distance (Rubincam, 2000; Scheeres, 2007). Thus, if rotational-fission mechanism or rotational re-arrangement is also several times more effective to create Q-type NEAs than Q-type MBAs, it may be able to explain why the Q/S ratio in NEAs is about 10 to 40 times larger than Q/S ratio in MBAs.

The YORP spin-up can also explain the existence of main-belt Q-type asteroids (see Polishook et al. (2014) for detail). It indicates the size-color (or size-S/Q ratio) dependence of S-complex MBAs, because the smaller asteroid is easier to be accelerated to near the break-up limit resulting in the Q-type-like color. However, such relation is not shown in our sample. There are two possible effects that may cause the lack of size dependence:

1. The “secondary fission” of rotational-fission models provided by Jacobson and Scheeres (2011) may be the more likely model to create main-belt Q-type asteroids. This model implies the destruction of the secondary of pair asteroids by primary’s tidal forces. For the km to sub-km sized asteroid pair, the gravity may be too small to deform secondary and produce Q-type surface.
2. A size-dependent strength for asteroids in addition to gravity (Holsapple, 2007) can prevent the break-up of small asteroids. The existence of sub-km sized super-fast rotator, such as (29075) 1950 DA (Rozitis et al., 2014) and (335433) 2005 UW163 (Chang et al., 2014), might be the evidence of the existence of this internal strength.

The other mechanism is thermal degradation of the rocks on asteroid surface from Delbo et al. (2014). This process is strongly dependent on the value of diurnal temperature difference, which is a function of perihelion distance; it takes $\sim 10^5$ yrs in near Earth region and $\sim 10^7$ yrs in the main-belt to break 90% of 3 centimeter diameter size rocks. If thermal degradation dominates the formation of Q-type asteroids, space weathering must have timescale $< 10^7$ yrs to keep low Q/S ratio in the main-belt.

5. Summary

We surveyed kilometer- to sub-kilometer-sized asteroids in the main belt by using the Subaru telescope. A total of 150 asteroids with BVRI colors

were detected and 75 of them exhibited satisfactory photometry accuracy. The main results can be summarized as follows:

1. Q-type asteroids are rare in the main-belt; only two Q-type candidates were detected in our sample, and the Q-type to S-type ratio is less than 0.05 in main-belt.
2. Unlike the size-color dependence of NEAs found by Dandy et al. (2003), we did not find any evidence of that in MBA population.
3. The space weathering timescale in the main belt should be less than 10^8 years.
4. Re-arrangement of surface material of S-type asteroid by tidal stress during planetary encounters and thermal degradation are possible mechanisms of Q-type NEAs formation. YORP spin-up induced rotational-fission or surface re-arrangement of asteroids could be responsible for both Q-type MBAs and NEAs formation.

Acknowledgments

We also acknowledge the anonymous referees' useful suggestions for improving the manuscript. This work is based on data collected at Subaru Telescope, which is operated by the National Astronomical Observatory of Japan. This work was supported in part by NSC Grant: NSC 101-2119-M-008-007-MY3 and NSC 102-2119-M-008-001. The Pan-STARRS1 Surveys (PS1) have been made possible through contributions by the Institute for Astronomy, the University of Hawaii, the Pan-STARRS Project Office, the Max-Planck Society and its participating institutes, the Max Planck Institute for Astronomy, Heidelberg and the Max Planck Institute for Extraterrestrial Physics, Garching, The Johns Hopkins University, Durham University, the University of Edinburgh, the Queen's University Belfast, the Harvard-Smithsonian Center for Astrophysics, the Las Cumbres Observatory Global Telescope Network Incorporated, the National Central University of Taiwan, the Space Telescope Science Institute, and the National Aeronautics and Space Administration under Grant No. NNX08AR22G issued through the Planetary Science Division of the NASA Science Mission Directorate, the National Science Foundation Grant No. AST-1238877, the University of Maryland, Eotvos Lorand University (ELTE), and the Los Alamos National Laboratory.

References

- Bernstein, G., Khushalani, B. 2000. Orbit Fitting and Uncertainties for Kuiper Belt Objects. *The Astronomical Journal* 120, 3323-3332.
- Binzel, R. P., Xu, S., Bus, S. J., Skrutskie, M. F., Meyer, M. R., Knezek, P., Barker, E. S. 1993. Discovery of a Main-Belt Asteroid Resembling Ordinary Chondrite Meteorites. *Science* 262, 1541-1543.
- Binzel, R. P., Bus, S. J., Burbine, T. H., Sunshine, J. M. 1996. Spectral Properties of Near-Earth Asteroids: Evidence for Sources of Ordinary Chondrite Meteorites. *Science* 273, 946-948.
- Binzel, R. P., Harris, A. W., Bus, S. J., Burbine, T. H. 2001. Spectral Properties of Near-Earth Objects: Palomar and IRTF Results for 48 Objects Including Spacecraft Targets (9969) Braille and (10302) 1989 ML. *Icarus* 151, 139-149.
- Binzel, R. P., Rivkin, A. S., Stuart, J. S., Harris, A. W., Bus, S. J., Burbine, T. H. 2004. Observed spectral properties of near-Earth objects: results for population distribution, source regions, and space weathering processes. *Icarus* 170, 259-294.
- Binzel, R. P., Morbidelli, A., Merouane, S., DeMeo, F. E., Birlan, M., Vernazza, P., Thomas, C. A., Rivkin, A. S., Bus, S. J., Tokunaga, A. T. 2010. Earth encounters as the origin of fresh surfaces on near-Earth asteroids. *Nature* 463, 331-334.
- Bottke, W. F., Jr., Nolan, M. C., Greenberg, R. 1993. Collision lifetimes and impact statistics of near-Earth asteroids. *Lunar and Planetary Science Conference* 24, 159-160.
- Bottke, W. F., Nolan, M. C., Greenberg, R., Kolvoord, R. A. 1994. Velocity distributions among colliding asteroids. *Icarus* 107, 255-268.
- Bottke, W. F., Morbidelli, A., Jedicke, R., Petit, J.-M., Levison, H. F., Michel, P., Metcalfe, T. S. 2002. Debiased Orbital and Absolute Magnitude Distribution of the Near-Earth Objects. *Icarus* 156, 399-433.
- Bottke, W. F., Durda, D. D., Nesvorný, D., Jedicke, R., Morbidelli, A., Vokrouhlický, D., Levison, H. 2005. The fossilized size distribution of the main asteroid belt. *Icarus* 175, 111-140.

- Bottke, W. F., Durda, D. D., Nesvorný, D., Jedicke, R., Morbidelli, A., Vokrouhlický, D., Levison, H. F. 2005. Linking the collisional history of the main asteroid belt to its dynamical excitation and depletion. *Icarus* 179, 63-94.
- Bowell, E., Chapman, C. R., Gradie, J. C., Morrison, D., Zellner, B. 1978. Taxonomy of asteroids. *Icarus* 35, 313-335.
- Bowell, E., Lumme, K. 1979. Colorimetry and magnitudes of asteroids. *Asteroids* 132-169.
- Brunetto, R., Vernazza, P., Marchi, S., Birlan, M., Fulchignoni, M., Orofino, V., Strazzulla, G. 2006. Modeling asteroid surfaces from observations and irradiation experiments: The case of 832 Karin. *Icarus* 184, 327-337.
- Bus, S. J., Binzel, R. P. 2002. Phase II of the Small Main-Belt Asteroid Spectroscopic Survey. The Observations. *Icarus* 158, 106-145.
- Bus, S. J., Binzel, R. P. 2002. Phase II of the Small Main-Belt Asteroid Spectroscopic Survey. A Feature-Based Taxonomy. *Icarus* 158, 146-177.
- Carvano, J. M., Hasselmann, P. H., Lazzaro, D., Mothé-Diniz, T. 2010. SDSS-based taxonomic classification and orbital distribution of main belt asteroids. *Astronomy and Astrophysics* 510, AA43.
- Chang, C.-K., Waszczak, A., Lin, H.-W., Ip, W.-H., Prince, T. A., Kulkarni, S. R., Laher, R., Surace, J. 2014. A New Large Super-fast Rotator: (335433) 2005 UW163. *The Astrophysical Journal* 791, L35.
- Chapman, C. R. 1996. S-Type Asteroids, Ordinary Chondrites, and Space Weathering: The Evidence from Galileo's Fly-bys of Gaspia and Ida. *Meteoritics and Planetary Science* 31, 699-725.
- Chapman, C. R. 2004. Space Weathering of Asteroid Surfaces. *Annual Review of Earth and Planetary Sciences* 32, 539-567.
- Chapman, C. R. 2010. Asteroids: Stripped on passing by Earth. *Nature* 463, 305-306.
- Clark, B. E., and 11 colleagues 2001. Space weathering on Eros: Constraints from albedo and spectral measurements of Psyche crater. *Meteoritics and Planetary Science* 36, 1617-1637.

- Clark, B. E., Helfenstein, P., Bell, J. F., Peterson, C., Veverka, J., Izenberg, N. I., Domingue, D., Wellnitz, D., McFadden, L. 2002. NEAR Infrared Spectrometer Photometry of Asteroid 433 Eros. *Icarus* 155, 189-204.
- Dandy, C. L., Fitzsimmons, A., Collander-Brown, S. J. 2003. Optical colors of 56 near-Earth objects: trends with size and orbit. *Icarus* 163, 363-373.
- Davis, D. R., Durda, D. D., Marzari, F., Campo Bagatin, A., Gil-Hutton, R. 2002. Collisional Evolution of Small-Body Populations. *Asteroids III* 545-558.
- Delbo, M., Libourel, G., Wilkerson, J., Murdoch, N., Michel, P., Ramesh, K. T., Ganino, C., Verati, C., Marchi, S. 2014. Thermal fatigue as the origin of regolith on small asteroids. *Nature* 508, 233-236.
- DeMeo, F. E., Binzel, R. P., Slivan, S. M., Bus, S. J. 2009. An extension of the Bus asteroid taxonomy into the near-infrared. *Icarus* 202, 160-180.
- DeMeo, F. E., Carry, B. 2013. The taxonomic distribution of asteroids from multi-filter all-sky photometric surveys. *Icarus* 226, 723-741.
- DeMeo, F. E., Carry, B. 2014. Solar System evolution from compositional mapping of the asteroid belt. *Nature* 505, 629-634.
- DeMeo, F. E., Binzel, R. P., Lockhart, M. 2014. Mars encounters cause fresh surfaces on some near-Earth asteroids. *Icarus* 227, 112-122.
- Hapke, B. 2001. Space weathering from Mercury to the asteroid belt. *Journal of Geophysical Research* 106, 10039-10074.
- Holmberg, J., Flynn, C., Portinari, L. 2006. The colours of the Sun. *Monthly Notices of the Royal Astronomical Society* 367, 449-453.
- Holsapple, K. A. 2007. Spin limits of Solar System bodies: From the small fast-rotators to 2003 EL61. *Icarus* 187, 500-509.
- Ishiguro, M., and 18 colleagues 2007. Global mapping of the degree of space weathering on asteroid 25143 Itokawa by Hayabusa/AMICA observations. *Meteoritics and Planetary Science* 42, 1791-1800.

- Ivezić, Ž., and 32 colleagues 2001. Solar System Objects Observed in the Sloan Digital Sky Survey Commissioning Data. *The Astronomical Journal* 122, 2749-2784.
- Jacobson, S. A., Scheeres, D. J. 2011. Dynamics of rotationally fissioned asteroids: Source of observed small asteroid systems. *Icarus* 214, 161-178.
- Jedicke, R., Nesvorný, D., Whiteley, R., Ivezić, Ž., Jurić, M. 2004. An age-colour relationship for main-belt S-complex asteroids. *Nature* 429, 275-277.
- Lantz, C., Clark, B. E., Barucci, M. A., Lauretta, D. S. 2013. Evidence for the effects of space weathering spectral signatures on low albedo asteroids. *Astronomy and Astrophysics* 554, A138.
- Lazzaro, D., Angeli, C. A., Carvano, J. M., Mothé-Diniz, T., Duffard, R., Florczak, M. 2004. S³OS²: the visible spectroscopic survey of 820 asteroids. *Icarus* 172, 179-220.
- Magnier, E. A., and 13 colleagues 2013. The Pan-STARRS 1 Photometric Reference Ladder, Release 12.01. *The Astrophysical Journal Supplement Series* 205, 20.
- Marchi, S., Magrin, S., Nesvorný, D., Paolicchi, P., Lazzarin, M. 2006. A spectral slope versus perihelion distance correlation for planet-crossing asteroids. *Monthly Notices of the Royal Astronomical Society* 368, L39-L42.
- Miglierini, F., Michel, P., Morbidelli, A., Nesvorný, D., Zappala, V. 1998. Origin of Multikilometer Earth- and Mars-Crossing Asteroids: A Quantitative Simulation. *Science* 281, 2022.
- Miyazaki, S., and 14 colleagues 2002. Subaru Prime Focus Camera – Suprime-Cam. *Publications of the Astronomical Society of Japan* 54, 833-853.
- Morbidelli, A., Vokrouhlický, D. 2003. The Yarkovsky-driven origin of near-Earth asteroids. *Icarus* 163, 120-134.
- Morbidelli, A., Bottke, W. F., Nesvorný, D., Levison, H. F. 2009. Asteroids were born big. *Icarus* 204, 558-573.
- Mothé-Diniz, T., Nesvorný, D. 2008. Visible spectroscopy of extremely young asteroid families. *Astronomy and Astrophysics* 486, L9-L12.

- Nakamura, T., Yoshida, F. 2002. Statistical Method for Deriving Spatial and Size Distributions of Sub-km Main-Belt Asteroids from Their Sky Motions. *Publications of the Astronomical Society of Japan* 54, 1079-1089.
- Nesvorný, D., Jedicke, R., Whiteley, R. J., Ivezić, Ž. 2005. Evidence for asteroid space weathering from the Sloan Digital Sky Survey. *Icarus* 173, 132-152.
- Nesvorný, D., Bottke, W. F., Vokrouhlický, D., Chapman, C. R., Rafkin, S. 2010. Do planetary encounters reset surfaces of near Earth asteroids?. *Icarus* 209, 510-519.
- Padmanabhan, N., and 23 colleagues 2008. An Improved Photometric Calibration of the Sloan Digital Sky Survey Imaging Data. *The Astrophysical Journal* 674, 1217-1233.
- Petit, J.-M., Holman, M. J., Gladman, B. J., Kavelaars, J. J., Scholl, H., Lored, T. J. 2006. The Kuiper Belt luminosity function from $m_R = 22$ to 25. *Monthly Notices of the Royal Astronomical Society* 365, 429-438.
- Polishook, D., Moskovitz, N., Binzel, R. P., DeMeo, F. E., Vokrouhlický, D., Žižka, J., Oszkiewicz, D. 2014. Observations of fresh and weathered surfaces on asteroid pairs and their implications on the rotational-fission mechanism. *Icarus* 233, 9-26.
- Rabinowitz, D. L. 1997. Are Main-Belt Asteroids a Sufficient Source for the Earth-Approaching Asteroids?. *Icarus* 127, 33-54.
- Rivkin, A. S., Thomas, C. A., Trilling, D. E., Enga, M.-t., Grier, J. A. 2011. Ordinary chondrite-like colors in small Koronis family members. *Icarus* 211, 1294-1297.
- Rozitis, B., MacLennan, E., Emery, J. P. 2014. Cohesive forces prevent the rotational breakup of rubble-pile asteroid (29075) 1950 DA. *Nature* 512, 174-176.
- Rubincam, D. P. 2000. Radiative Spin-up and Spin-down of Small Asteroids. *Icarus* 148, 2-11.
- Sasaki, S., Nakamura, K., Hamabe, Y., Kurahashi, E., Hiroi, T. 2001. Production of iron nanoparticles by laser irradiation in a simulation of lunar-like space weathering. *Nature* 410, 555-557.

- Schlaflly, E. F., and 16 colleagues 2012. Photometric Calibration of the First 1.5 Years of the Pan-STARRS1 Survey. *The Astrophysical Journal* 756, 158.
- Scheeres, D. J. 2007. The dynamical evolution of uniformly rotating asteroids subject to YORP. *Icarus* 188, 430-450.
- Scheeres, D. J. 2015. Landslides and Mass shedding on spinning spheroidal asteroids. *Icarus* 247, 1-17.
- Stuart, J. S., Binzel, R. P. 2004. Bias-corrected population, size distribution, and impact hazard for the near-Earth objects. *Icarus* 170, 295-311.
- Tholen, D. J. 1984. Asteroid taxonomy from cluster analysis of Photometry. Ph.D. Thesis .
- Thomas, C. A., Rivkin, A. S., Trilling, D. E., Enga, M.-t., Grier, J. A. 2011. Space weathering of small Koronis family members. *Icarus* 212, 158-166.
- Thomas, C. A., Trilling, D. E., Rivkin, A. S. 2012. Space weathering of small Koronis family asteroids in the SDSS Moving Object Catalog. *Icarus* 219, 505-507.
- Tonry, J. L., and 13 colleagues 2012. The Pan-STARRS1 Photometric System. *The Astrophysical Journal* 750, 99.
- Vereš, P., Jedicke, R., Denneau, L., Wainscoat, R., Holman, M. J., Lin, H.-W. 2012. Improved Asteroid Astrometry and Photometry with Trail Fitting. *Publications of the Astronomical Society of the Pacific* 124, 1197-1207.
- Vernazza, P., Binzel, R. P., Rossi, A., Fulchignoni, M., Birlan, M. 2009. Solar wind as the origin of rapid reddening of asteroid surfaces. *Nature* 458, 993-995.
- Walsh, K. J., Richardson, D. C., Michel, P. 2012. Spin-up of rubble-pile asteroids: Disruption, satellite formation, and equilibrium shapes. *Icarus* 220, 514-529.
- Willman, M., Jedicke, R., Nesvorný, D., Moskovitz, N., Ivezić, Ž., Fevig, R. 2008. Redetermination of the space weathering rate using spectra of Iannini asteroid family members. *Icarus* 195, 663-673.

- Willman, M., Jedicke, R., Moskovitz, N., Nesvorný, D., Vokrouhlický, D., Mothé-Diniz, T. 2010. Using the youngest asteroid clusters to constrain the space weathering and gardening rate on S-complex asteroids. *Icarus* 208, 758-772.
- Willman, M., Jedicke, R. 2011. Asteroid age distributions determined by space weathering and collisional evolution models. *Icarus* 211, 504-510.
- Yoshida, F., Nakamura, T. 2007. Subaru Main Belt Asteroid Survey (SM-BAS) - Size and color distributions of small main-belt asteroids. *Planetary and Space Science* 55, 1113-1125.
- Zellner, B., Tholen, D. J., Tedesco, E. F. 1985. The eight-color asteroid survey - Results for 589 minor planets. *Icarus* 61, 355-416.